

Accelerated Article Preview

The coding capacity of SARS-CoV-2

Received: 15 May 2020

Accepted: 1 September 2020

Accelerated Article Preview Published
online 9 September 2020

Cite this article as: Finkel, Y. et al. The
coding capacity of SARS-CoV-2. *Nature*
<https://doi.org/10.1038/s41586-020-2739-1>
(2020).

Yaara Finkel, Orel Mizrahi, Aharon Nachshon, Shira Weingarten-Gabbay, David Morgenstern,
Yfat Yahalom-Ronen, Hadas Tamir, Hagit Achdout, Dana Stein, Ofir Israeli, Adi Beth-Din,
Sharon Melamed, Shay Weiss, Tomer Israely, Nir Paran, Michal Schwartz &
Noam Stern-Ginossar

This is a PDF file of a peer-reviewed paper that has been accepted for publication.
Although unedited, the content has been subjected to preliminary formatting. Nature
is providing this early version of the typeset paper as a service to our authors and
readers. The text and figures will undergo copyediting and a proof review before the
paper is published in its final form. Please note that during the production process
errors may be discovered which could affect the content, and all legal disclaimers
apply.

The coding capacity of SARS-CoV-2

<https://doi.org/10.1038/s41586-020-2739-1>

Received: 15 May 2020

Accepted: 1 September 2020

Published online: 9 September 2020

Yaara Finkel^{1,7}, Orel Mizrahi^{1,7}, Aharon Nachshon¹, Shira Weingarten-Gabbay^{2,3}, David Morgenstern⁴, Yfat Yahalom-Ronen⁵, Hadas Tamir⁵, Hagit Achdout⁵, Dana Stein⁶, Ofir Israeli⁶, Adi Beth-Din⁶, Sharon Melamed⁵, Shay Weiss⁵, Tomer Israely⁵, Nir Paran⁵, Michal Schwartz¹ & Noam Stern-Ginossar¹✉

Severe acute respiratory syndrome coronavirus 2 (SARS-CoV-2) is the cause of the ongoing Coronavirus disease 19 (COVID-19) pandemic¹. In order to understand SARS-CoV-2 pathogenicity and antigenic potential, and to develop therapeutic tools, it is essential to portray the full repertoire of its expressed proteins. The SARS-CoV-2 coding capacity map is currently based on computational predictions and relies on homology to other coronaviruses. Since coronaviruses differ in their protein array, especially in the variety of accessory proteins, it is crucial to characterize the specific collection of SARS-CoV-2 proteins in an unbiased and open-ended manner. Using a suite of ribosome profiling techniques^{2–4}, we present a high-resolution map of the SARS-CoV-2 coding regions, allowing us to accurately quantify the expression of canonical viral open reading frames (ORFs) and to identify 23 unannotated viral ORFs. These ORFs include upstream ORFs (uORFs) that are likely playing a regulatory role, several in-frame internal ORFs lying within existing ORFs, resulting in N-terminally truncated products, as well as internal out-of-frame ORFs, which generate novel polypeptides. We further show that viral mRNAs are not translated more efficiently than host mRNAs; rather, virus translation dominates host translation due to high levels of viral transcripts. Our work provides a rich resource, which will form the basis of future functional studies.

SARS-CoV-2 is an enveloped virus consisting of a positive-sense, single-stranded RNA genome of ~30kb. Two overlapping ORFs, ORF1a and ORF1b, are translated from the positive strand genomic RNA and generate continuous polypeptides which are cleaved into a total of 16 nonstructural proteins (NSPs). The translation of ORF1b is mediated by a -1 frameshift that allows translation to continue beyond the stop codon of ORF1a. From the viral genome, negative-strand RNA intermediates are produced and serve as templates for the synthesis of positive-strand genomic RNA and of subgenomic RNAs⁵. The subgenomic RNAs contain a common 5' leader fused to different segments from the 3' end of the viral genome, and contain a 5'-cap structure and a 3' poly(A) tail^{6,7}. These unique fusions occur during negative-strand synthesis at 6–7 nt core sequences called transcription-regulating sequences (TRS)s that are located at the 3' end of the leader sequence as well as preceding each viral ORF. The different subgenomic RNAs encode 4 conserved structural proteins- spike (S), envelope (E), membrane (M), nucleocapsid (N)- and several accessory proteins. Based on sequence similarity to other beta coronaviruses and specifically to SARS-CoV, current annotation of SARS-CoV-2 includes predictions of six accessory proteins (3a, 6, 7a, 7b, 8, and 10, NC_045512.2), but not all were experimentally confirmed^{8,9}.

To capture the full SARS-CoV-2 coding capacity, we applied a suite of ribosome profiling approaches to Vero cells infected with SARS-CoV-2 for 5 or 24 h (Fig. 1a). At 24 h post infection (hpi) the vast majority of cells

were infected and cells were still intact (Extended data Fig. 1). For each time point we prepared three different ribosome-profiling libraries (Ribo-seq), each one in two biological replicates. Two Ribo-seq libraries facilitate mapping of translation initiation sites, by treating cells with lactimidomycin (LTM) or harringtonine (Harr), two drugs with distinct mechanisms that prevent 80S ribosomes at translation initiation sites from elongating. These treatments lead to strong accumulation of ribosomes precisely at the sites of translation initiation and depletion of ribosomes over the body of the ORF (Fig. 1a). The third Ribo-seq library was prepared from cells treated with the translation elongation inhibitor cycloheximide (CHX), and gives a snap-shot of actively translating ribosomes across the body of the translated ORF (Fig. 1a). In parallel, RNA-sequencing (RNA-seq) was applied to map viral transcripts. Analysis of cellular genes from the different Ribo-seq libraries revealed the expected distinct profiles in both replicates. Ribosome footprints displayed a strong peak at the translation initiation site, which, as expected, is more pronounced in the Harr and LTM libraries, while the CHX library also exhibited a distribution of ribosomes across the entire coding region, and its mapped footprints were enriched in fragments that align to the translated frame (Fig. 1b and Extended data Fig. 2a). As expected, the RNA-seq reads were uniformly distributed across coding and non-coding regions (Fig. 1b). The footprint profiles of viral coding sequences at 5 hpi fit the expected profile of translation (Fig. 1c, Extended data Fig. 2b) and the footprint densities were highly

¹Department of Molecular Genetics, Weizmann Institute of Science, Rehovot, 76100, Israel. ²Broad Institute of MIT and Harvard, Cambridge, MA, 02142, USA. ³Department of Organismal and Evolutionary Biology, Harvard University, Cambridge, MA, 02138, USA. ⁴de Botton Institute for Protein Profiling, The Nancy and Stephen Grand Israel National Center for Personalised Medicine, Weizmann Institute of Science, Rehovot, 76100, Israel. ⁵Department of Infectious Diseases, Israel Institute for Biological Research, Ness Ziona, 74100, Israel. ⁶Department of Biochemistry and Molecular Genetics, Israel Institute for Biological Research, Ness Ziona, 74100, Israel. ⁷These authors contributed equally: Yaara Finkel, Orel Mizrahi.

✉e-mail: noam.stern-ginossar@weizmann.ac.il

reproducible between biological replicates, at single nucleotide resolution (Extended data Fig. 2c). Intriguingly, the footprint profile over the viral genome at 24 hpi, did not fit the expected profile of translating ribosomes and were generally not affected by Harr or LTM treatments (Extended data Fig. 2b). To further examine the characteristics of the footprints, we applied a fragment length organization similarity score (FLOSS) that measures the magnitude of disagreement between the footprint distribution on a given transcript and the footprint distribution on canonical CDSs¹⁰. At 5 hpi protected fragments from SARS-CoV-2 ORFs did not differ from well-expressed cellular transcripts (Fig. 1d). However, reads from 24 hpi could be clearly distinguished from cellular CDSs (Fig. 1e). We conclude that the footprint data from 5 hpi constitutes robust and reproducible ribosome footprint information but that viral protected fragments at 24 hpi may reflect additional interactions with viral RNA that occur at late time points in infection.

A global view of RNA and CHX footprint reads mapping to the viral genome at 5 hpi, demonstrate RNA levels are constant across ORFs 1a and 1b, and steadily increase towards the 3', reflecting the cumulative abundance of these sequences due to the nested transcription of subgenomic RNAs (Fig. 2a). Increased coverage is also seen at the 5' UTR reflecting the presence of the 5' leader sequence in all subgenomic RNAs as well as the genomic RNA. Reduction in footprint density between ORF1a and ORF1b reflects the proportion of ribosomes that terminate at the ORF1a stop codon instead of frameshifting into ORF1b (Extended data Fig. 3). By dividing the footprint density in ORF1b by the density in ORF1a we estimate frameshift efficiency is 57% +/- 12%. This value is comparable to the frameshift efficiency measured based on ribosome profiling of mouse hepatitis virus (MHV, 48–75%)³. Similarly to what was seen in MHV and avian infectious bronchitis virus (IBV)^{3,11}, we failed to see noticeable ribosome pausing before or at the frameshift site, but we identified several potential pausing sites within ORF1a and in ORF1b (Extended data Fig. 3).

Besides ORF1a and ORF1b, all other canonical viral ORFs are translated from subgenomic RNAs. Since raw RNA-seq densities represent the cumulative sum of genomic and subgenomic RNAs, we calculated transcript abundance using two approaches: deconvolution of RNA densities, in which RNA expression of each ORF is calculated by subtracting the RNA read density of cumulative densities upstream to the ORF region; and relative abundances of RNA reads spanning leader-body junctions of each of the canonical subgenomic RNAs. For the majority of the ORFs there was high correlation between these two approaches (Pearson's R = 0.897, Extended data Fig. 4a), and in both approaches the N transcript was the most abundant transcript, in agreement with recent studies^{9,12}. We next compared footprint densities to RNA abundance. For the majority of viral ORFs, transcript abundance correlated almost perfectly with footprint densities (Fig. 2b), indicating these viral ORFs are translated in similar efficiencies (probably due to their almost identical 5'UTRs), however three ORFs were outliers. The translation efficiency of ORF1a and ORF1b was significantly lower. This can stem from unique features in their 5'UTR (discussed below) or from under estimation of their true translation efficiency as some of the full-length RNA molecules may serve as template for replication or packaging and are hence not part of the translated mRNA pool. The third outlier is ORF7b for which we identified very few body-leader junctions but it exhibited relatively high translation, likely due to ribosome leaky scanning of the ORF7a transcript, as was suggested in SARS-CoV¹³.

Recently, many transcripts derived from non-canonical junctions were identified for SARS-CoV-2^{9,12}. These junctions contain either the leader combined with 3' fragments at unexpected sites in the middle of ORFs (leader-dependent noncanonical junction) or fusion between sequences that do not have similarity to the leader (leader-independent junction). We estimated the frequency of junction-spanning reads in our RNA libraries and obtained excellent agreement between our replicates (Extended data Fig. 4b and c and Supplementary Table 1) and significant correlation with previous data from Vero cells¹² (Pearson's

R = 0.81, Extended data Fig. 4d), illustrating many of these junctions are reproducible between experimental systems. We also identified five abundant leader-independent junctions that were unique to our data (Supplementary Table 2). We noticed three of these junctions represent short in-frame deletions in the spike protein that overlap deletions in the furin-like cleavage site that were recently described⁹ (Extended data Fig. 4e). The re-occurrence of the same genomic deletion supports the conclusion that this deletion is being selected for during passage in Vero cells. To examine if additional non-canonical junctions are derived from genomic deletions we sequenced the genomic RNA of the virus we used in our infections. In addition to the deletions in the furin-like cleavage site, we identified an 8aa deletion in ORF-E in 2.3% of the genomic RNA (Supplementary Table 2 and Fig. 2c). When we compared the frequency of junctions between 5h and 24h time points, the leader-dependent junctions and the genomic deletions correlated well but the leader-independent junctions were specifically increased at 24 hpi (Fig. 2c). This data shows a small part of the leader-independent junctions represent genomic deletions and a larger subset rises at late stages of infection when genome replication is dominant and therefore likely do not significantly affect viral transcripts and translated ORFs.

Examination of SARS-CoV-2 translation as reflected by the diverse ribosome footprint libraries, revealed unannotated translated ORFs. We detected in-frame internal ORFs lying within existing ORFs, resulting in N-terminally truncated product. These include relatively long truncated versions of canonical ORFs, such as the one found in ORF6 (Fig. 3a and Extended data Fig. 5a), or very short truncated ORFs that may serve an upstream ORF (uORF), like truncated ORF7a that might regulate ORF7b translation (Fig. 3b, Extended data Fig. 5b). We also detected internal out-of-frame translations, that would yield novel polypeptides, such as ORFs within ORF3a (41aa and 33aa, Fig. 3c and Extended data Fig. 5c) and within ORF-S (39aa, Fig. 3d and Extended data Fig. 5d) or short ORFs that likely serve as uORFs (Fig. 3e and Extended data Fig. 5e). Additionally, we observed a 13 amino acid extended ORF-M, in addition to the canonical ORF-M, which is predicted to start at the near cognate codon AUA (Fig. 3f and Extended data Fig. 5f).

The presence of the annotated ORF10 was recently put into question as almost no subgenomic reads were found for its corresponding transcript^{12,14}. Although we also did not detect subgenomic RNA designated for ORF10 translation (Supplementary Table 1), the ribosome footprint densities indicate translation initiation signal in ORF10 (Fig. 3g and Extended data Fig. 5g). Interestingly, we detected two putative ORFs, an upstream out of frame ORF that overlaps ORF10 initiation and an in-frame internal initiation that leads to a truncated ORF10 product. Further research is needed to delineate how ORFs in this region are translated and whether they have any functional roles.

Finally, we detected four distinct initiation sites at SARS-CoV-2 5'UTR. Three of these encode for uORFs that are located just upstream of ORF1a; the first initiating at an AUG (uORF1) and the other two at a near cognate codons (uORF2 and extended uORF2, Fig. 3h and Extended data Fig. 5h). These uORFs are in line with findings in other coronaviruses^{3,15}. The fourth site is the most prominent peak in the ribosome profiling densities on the SARS-CoV-2 genome and is located on a CUG codon at position 59, just 10 nucleotides upstream the TRS-leader (Fig. 3i and Extended data Fig. 5i). The reads mapped to this site have a tight length distribution characteristic of ribosome protected fragments (Extended data Fig. 6a). The occupancy at the CUG is higher than the downstream translation signal (Fig. 3i), implying this peak might reflect ribosomal pausing. Due to its location upstream of the TRS-leader, footprints mapping to this site can potentially derive from any of the subgenomic as well as the genomic RNAs. Therefore, to view this initiation in its context, we aligned the footprints to the genomic RNA or to the most abundant subgenomic N transcript. On the genome and on ORF-N transcript this initiation results in translation of uORFs, which on the genome will generate an extension of uORF1 (Extended data Fig. 6b and c). Interestingly, ribosome pauses located just upstream

Article

of the TRS-leader were also identified in MHV and IBV genomes^{3,11}. To assess the distribution of footprints at this initiation on the different viral transcripts, viral transcripts were divided into three groups based on their sequence similarity downstream of the leader-junction site (to allow unique footprint alignment, Extended data Fig. 6d). Interestingly, significantly more footprints were mapped to the group that includes the genomic RNA and the subgenomic E and M transcripts, than would be expected from their relative RNA abundance (Extended data Fig. 6e). When only footprints that allow unique mapping to genomic RNA or subgenomic M and E transcripts are used (sizes 31–33bp to discriminate M from genome or E transcript, and sizes 32–33bp to discriminate E from the genome) a strong enrichment of footprints that originate from the genome is observed (Figure Extended data Fig. 6f). This footprint enrichment to genomic RNA suggests ribosome pausing might be more prominent on the genome or that ribosomes engage with genomic RNA differently than with subgenomic transcripts. The proximity of this pause to the leader-TRS, which seems to be conserved in MHV and IBV^{3,11}, together with the relative enrichment to the viral genome raises the possibility that a ribosome at this position might affect discontinuous transcription either by sterically blocking the TRS-L site or by affecting RNA secondary structure. In addition, ribosomes initiating at the CUG have the potential to generate uORFs or ORF extensions in the different sub-genomic transcripts (Supplementary Table 3).

To systematically define the SARS-CoV-2 translated ORFs we used PRICE and ORF-RATER, two computational methods that rely on a combination of translation features to predict novel translated ORFs from ribosome profiling measurements^{16,17}. After application of a minimal expression cutoff and manual curation on the predictions, these classifiers identified 25 ORFs, these included 10 out of the 11 canonical translation initiations and 15 novel viral ORFs. In addition, ORF-RATER identified three putative ORFs that originate from the CUG initiation and extend to the sub-genomic transcripts of S, M and ORF6 (Supplementary Table 3). The majority (85%) of the classifier identified ORFs were independently identified in each of the biological replicate (Supplementary Table 4). Visual inspection of the ribosome profiling data suggested additional 8 putative novel ORFs, some of which are presented above (Fig. 3a, 3b, 3g and Supplementary Table 4). Overall, we identified 23 putative ORFs, on top of the 12 canonical viral ORFs that are currently annotated in NCBI and 3 additional potential ORFs that stem from the CUG initiation upstream of the leader.

To confirm the robustness of these annotations we extended these experiments to human cells. We first examined the infection efficiency of several human cell lines that were used to study SARS-CoV-2 infection: Calu3, A549, and Caco-2. Infection of Calu3 was most efficient and infection in the presence of trypsin increased infection efficiency by at least twofold (Extended data Fig. 7a). We infected Calu3 with a different SARS-CoV-2 isolate, which was sequenced to confirm its integrity. The same set of ribosome profiling techniques were applied to cells at 7hpi, each in two biological replicates, in parallel with RNA-seq. The different Ribo-seq libraries showed the expected distinct profiles in both replicates, confirming the overall quality of these libraries (Extended data Fig. 7b). We examined the translation of the new viral ORFs; all 23 novel ORFs we identified as being translated in Vero cells showed evidence of translation also in Calu3 infected cells, 16 were annotated by PRICE and ORF-RATER (Extended data Fig. 8 and Supplementary Table 4). Also here ORF-RATER identified the same three ORFs that originate from the CUG initiation upstream the leader (Supplementary Table 3). LTM-induced ribosome accumulation at the canonical and predicted initiation sites were highly reproducible between biological replicates as well as between Calu3 and Vero cells (Extended data Fig. 9a-c). Furthermore, ribosome-protected footprints displayed a 3-nt periodicity that was in phase with the predicted start site, in both Vero and Calu3 cells providing further evidence for the active translation of the predicted ORFs (Extended data Fig. 9d). We conclude 23 unannotated ORFs are reproducibly translated from SARS-CoV-2 independently of

the host cell and the viral origin and additional ORFs may be translated from the CUG initiation located upstream of the TRS-leader.

Ribosome density also allows accurate quantification of viral protein production. We first quantified the relative expression levels of canonical viral ORFs based on the non-overlapping regions. ORF-N is expressed at the highest level in both Vero and Calu3 cells followed by the rest of the viral ORFs with some differences in the relative expression between the two cell types (Fig. 4a). To quantify the expression of out-of-frame internal ORFs we computed the contribution of the internal ORF to the frame periodicity signal relative to the expected contribution of the main ORF. For in-frame internal ORF quantification, we subtracted the coverage of the main ORF in the non-overlapping region. We also used ORF-RATER, which uses a regression strategy to calculate relative expression of overlapping ORFs, resulting in largely similar estimates of translation levels (Extended data Fig. 10a and b). These measurements show that many of the novel ORFs we annotated are expressed in comparable levels to the canonical ORFs (Fig. 4b and Supplementary Table 5). Furthermore, the relative expression of viral proteins seems to be mostly independent of the host cell origin (Fig. 4c).

Of the novel ORFs we identified 14 are very short (≤ 20 codons) or located in the 5'UTR of the genomic RNA and therefore likely play a regulatory role and three are extensions or truncations of canonical ORFs (M, 6 and 7a). We examined the properties of the six out-of-frame internal ORFs (iORF)s that are longer than 20aa; one of these ORFs is ORF9b and its truncated version (Extended data Fig. 10c and d, 97aa and 90aa). ORF9b appears in UniProt annotations and was detected by Bojkova et al.⁸ in proteomic measurements, together with our translation measurements this indicates it is a bona fide SARS-CoV-2 protein. In addition we detected an iORF at the 5' of ORF-S and its truncated version (Fig. 3d, 39 aa and 31 aa), and two iORFs within ORF3a (Fig. 3c, 41aa and 33aa). Mining proteomic measurements of SARS-CoV-2 infected cells^{8,9} did not detect peptides that originate from these out-of-frame ORFs, likely due to challenges in detecting trypsin-digested products from short coding regions¹⁶. Indeed, two canonical SARS-CoV-2 proteins, ORF7b (43aa) and ORF-E (75aa) were also not detected by mass-spectrometry^{8,9}, and our ribosome profiling data are the first to show these SARS-CoV-2 proteins are indeed expressed.

S.iORF1 and 3a.iORF1 are predicted to contain a transmembrane domain (Extended data Fig. 10e and f) and 3a.iORF2 contain a predicted signal peptide (Extended data Fig. 10g). Analysis of the conservation of these out-of-frame iORFs in SARS-CoV and in related viruses (Sarbecoviruses) revealed 3a.iORF1 is highly conserved (Supplementary Table 6). This ORF was also identified by three independent comparative genomic studies that demonstrate it has a significant purifying selection signature, implying it is a functional polypeptide^{18–20}. In combination, these findings indicate 3a.iORF1 is a functional transmembrane protein, conserved throughout sarbecoviruses and should be named ORF3c^{19,20}. The second iORF overlapping ORF3a (3a.iORF2) and the iORF overlapping S (S.iORF1) are not conserved in most sarbecoviruses (Supplementary Table 6 and 19). The expression of 3a.iORF2 is low (Fig. 4b and Extended data Fig. 9d) and an extended version of this ORF was pulled-down²¹ and was shown to elicit an antibody response²² but we find mainly translation of the truncated version (Extended data Fig. 10h and i). The internal S-ORF (S.iORF1) is situated just downstream of ORF-S AUG, suggesting ribosomes might initiate translation via leaky scanning. This region in the S-protein shows extremely-rapid evolution²⁰ but in the SARS-CoV-2 isolates that have been sequenced its coding capacity is maintained²³. Future work will have to delineate if this ORF, which is highly expressed (Fig. 4b), represents a functional transmembrane protein. Importantly, translated ORFs that do not act as functional polypeptides could still be an important part of the immunological repertoire of the virus as MHC class I bound peptides are generated at higher efficiency from rapidly degraded polypeptides²⁴.

Finally, although we identified two internal out-of-frame ORFs within ORF3a, we did not detect translation of SARS-CoV ORF3b homologue,

which contains a premature stop codon in SARS-CoV-2 (Extended data Fig. 10h and i). We also did not find evidence of translation of ORF14, which appears in some SARS-CoV-2 annotations¹⁵ (Extended data Fig. 10c and d).

Translation of viral proteins relies on the cellular translation machinery, and coronaviruses, like many other viruses, are known to cause host shutoff²⁵. In order to quantitatively evaluate if SARS-CoV-2 skews the translation machinery to preferentially translate viral transcripts, we compared the ratio of footprints to mRNAs for virus and host CDSs at 5 hpi and 24 hpi in Vero cells and at 7 hpi in Calu3 cells. Since at 24 hpi ribosome densities were masked by a contaminant signal, for samples from this time point we used the footprints that were mapped to subgenomic RNA junctions (and therefore reflect bona fide transcripts) to estimate ribosome densities. In all samples the virus translation efficiencies fall within the low range of most of the host genes (Fig. 4d–4f), indicating viral transcripts are not preferentially translated in infected cells. Instead, viral transcripts take over the mRNA pool, probably through massive transcription coupled to host induced RNA degradation^{26,27}.

In summary, in this study we delineate the translation landscape of SARS-CoV-2. Comprehensive mapping of the expressed ORFs is a prerequisite for the functional investigation of viral proteins and for deciphering viral-host interactions. An in-depth analysis of the ribosome profiling experiments demonstrated a highly complex landscape of translation products, including translation of 23 novel viral ORFs and revealed the relative production of canonical viral proteins. The new ORFs we have identified may serve as novel accessory proteins or as regulatory units controlling the balanced production of different viral proteins. Studies on the functional significance and antigenic potential of these ORFs will deepen our understanding of SARS-CoV-2 and of coronaviruses in general.

Online content

Any methods, additional references, Nature Research reporting summaries, source data, extended data, supplementary information, acknowledgements, peer review information; details of author contributions and competing interests; and statements of data and code availability are available at <https://doi.org/10.1038/s41586-020-2739-1>.

1. Zhu, N. et al. A novel coronavirus from patients with pneumonia in China, 2019. *N. Engl. J. Med.* **382**, 727–733 (2020).
2. Stern-Ginossar, N. et al. Decoding human cytomegalovirus. *Science* (80-.). **338**, 1088–1093 (2012).
3. Irigoyen, N. et al. High-Resolution Analysis of Coronavirus Gene Expression by RNA Sequencing and Ribosome Profiling. *PLoS Pathog.* **12**, e1005473 (2016).
4. Finkel, Y. et al. Comprehensive annotations of human herpesvirus 6A and 6B genomes reveal novel and conserved genomic features. *eLife* **9**, e50960 (2020).

5. Sola, I., Almazán, F., Zúñiga, S. & Enjuanes, L. Continuous and Discontinuous RNA Synthesis in Coronaviruses. *Annu. Rev. Virol.* **2**, 265–288 (2015).
6. Lai, M. M. & Stohlman, S. A. Comparative analysis of RNA genomes of mouse hepatitis viruses. *J. Virol.* **38**, 661–670 (1981).
7. Yogo, Y., Hirano, N., Hino, S., Shibuta, H. & Matumoto, M. Polyadenylate in the virion RNA of mouse hepatitis virus. *J. Biochem.* **82**, 1103–1108 (1977).
8. Bojkova, D. et al. Proteomics of SARS-CoV-2-infected host cells reveals therapy targets. *Nature* **583**, 469–472 (2020).
9. Davidson, A. D. et al. Characterisation of the transcriptome and proteome of SARS-CoV-2 reveals a cell passage induced in-frame deletion of the furin-like cleavage site from the spike glycoprotein. *Genome Med.* **12**, 68 (2020).
10. Ingolia, N. T. et al. Ribosome profiling reveals pervasive translation outside of annotated protein-coding genes. *Cell Rep.* **8**, 1365–1379 (2014).
11. Dinan, A. M. et al. Comparative Analysis of Gene Expression in Virulent and Attenuated Strains of Infectious Bronchitis Virus at Subcodon Resolution. *J. Virol.* **93**, 714–733 (2019).
12. Kim, D. et al. The architecture of SARS-CoV-2 transcriptome. *Cell* **S0092-8674**, 30406–2 (2020).
13. Schaecher, S. R., Mackenzie, J. M. & Pekosz, A. The ORF7b protein of severe acute respiratory syndrome coronavirus (SARS-CoV) is expressed in virus-infected cells and incorporated into SARS-CoV particles. *J. Virol.* **81**, 718–731 (2007).
14. Davidson, A. D. et al. Characterisation of the transcriptome and proteome of SARS-CoV-2 using direct RNA sequencing and tandem mass spectrometry reveals evidence for a cell passage induced in-frame deletion in the spike glycoprotein that removes the furin-like cleavage site. *bioRxiv* 2020.03.22.002204 (2020). <https://doi.org/10.1101/2020.03.22.002204>.
15. Wu, A. et al. Genome Composition and Divergence of the Novel Coronavirus (2019-nCoV) Originating in China. *Cell Host Microbe* **27**, 325–328 (2020).
16. Erhard, F. et al. Improved Ribo-seq enables identification of cryptic translation events. *Nat. Methods* **15**, 363–366 (2018).
17. Fields, A. P. et al. A Regression-Based Analysis of Ribosome-Profiling Data Reveals a Conserved Complexity to Mammalian Translation. *Mol. Cell* **60**, 816–827 (2015).
18. Cagliani, R., Forni, D., Clerici, M. & Sironi, M. Coding potential and sequence conservation of SARS-CoV-2 and related animal viruses. *Infect. Genet. Evol.* **83**, 104353 (2020).
19. Firth, A. E. A putative new SARS-CoV protein, 3c, encoded in an ORF overlapping ORF3a. *J. Gen. Virol.* **...**, jgv001469 (2020). 10.1099/jgv.0.001469.
20. Jungreis, I., Sealfon, R. & Kellis, M. Sarbecovirus comparative genomics elucidates gene content of SARS-CoV-2 and functional impact of COVID-19 pandemic mutations. *bioRxiv* 2020.06.02.130955 (2020). <https://doi.org/10.1101/2020.06.02.130955>.
21. Gordon, D. E. et al. A SARS-CoV-2 protein interaction map reveals targets for drug repurposing. *Nature* **583**, 459–468 (2020).
22. Hachim, A. et al. Beyond the Spike: identification of viral targets of the antibody response to SARS-CoV-2 in COVID-19 patients. *medRxiv* 2020.04.30.20085670 (2020). <https://doi.org/10.1101/2020.04.30.20085670>.
23. Hadfield, J. et al. Nextstrain: real-time tracking of pathogen evolution. *Bioinformatics* **34**, 4121–4123 (2018).
24. Yewdell, J. W. DRIPs solidify: progress in understanding endogenous MHC class I antigen processing. *Trends Immunol.* **32**, 548–558 (2011).
25. Abernathy, E. & Glaunsinger, B. Emerging roles for RNA degradation in viral replication and antiviral defense. *Virology* **479–480**, 600–608 (2015).
26. Huang, C. et al. SARS coronavirus nsp1 protein induces template-dependent endonuclease activity of mRNAs: viral mRNAs are resistant to nsp1-induced RNA cleavage. *PLoS Pathog.* **7**, e1002433 (2011).
27. Kamitani, W., Huang, C., Narayanan, K., Lokugamage, K. G. & Makino, S. A two-pronged strategy to suppress host protein synthesis by SARS coronavirus Nsp1 protein. *Nat. Struct. Mol. Biol.* **16**, 1134–1140 (2009).

Publisher's note Springer Nature remains neutral with regard to jurisdictional claims in published maps and institutional affiliations.

© The Author(s), under exclusive licence to Springer Nature Limited 2020

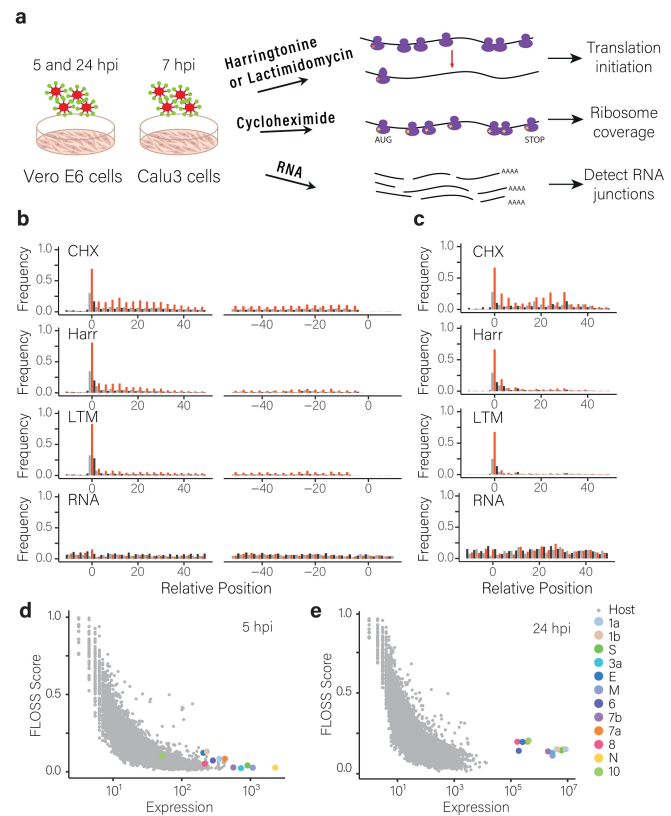


Fig. 1 | Ribosome profiling of SARS-CoV-2 infected cells. (A) Vero and Calu3 cells infected with SARS-CoV-2 were harvested at 5, 24 (Vero) and 7 (Calu3) hpi for RNA-seq, and for Ribo-seq using lactimidomycin, Harringtonine or cycloheximide treatments. (B) Metagene analysis of read densities around the start and stop codons of cellular CDSs at 5 hpi. The ribosome densities are shown with different colours indicating the three frames (red, 0; black, +1; grey, +2). (C) Metagene analysis around the start codon, as described in B, for viral ORFs at 5 hpi. (D and E) FLOSS score for cellular and SARS-CoV-2 ORFs at 5 hpi (D) and 24 hpi (E).

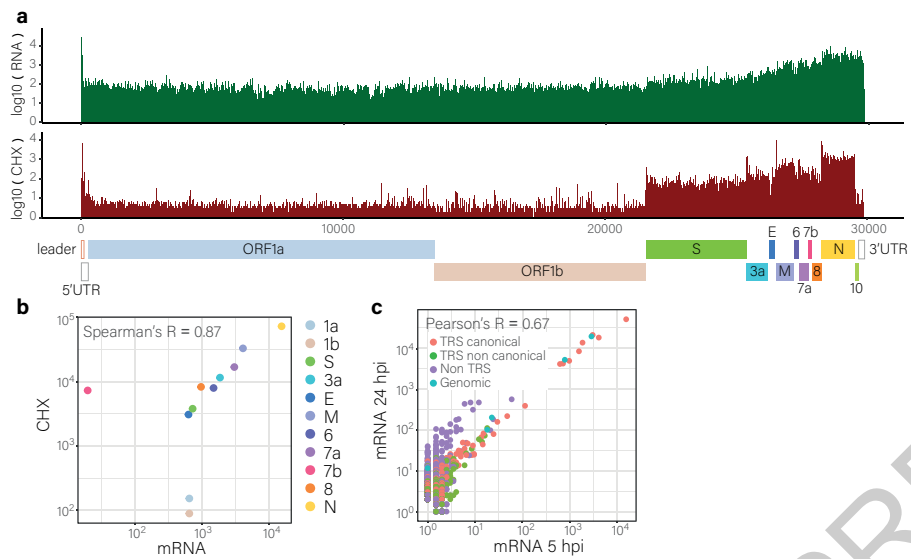


Fig. 2 | Expression level of canonical viral ORFs. (A) RNA-Seq (green) and Ribo-Seq CHX (red) read densities at 5 hpi along the SARS-CoV-2 genome. SARS-CoV-2 canonical ORFs are labelled (B) Transcript abundance relative to ribosome densities of each SARS-CoV-2 canonical ORF at 5 hpi. (C) Scatter plot

of the abundance of reads that span canonical leader-dependent junctions (red), non-canonical leader-dependent junctions (green), non-canonical leader-independent junctions (purple) or genomic deletions (cyan) at 5 and 24 hpi.

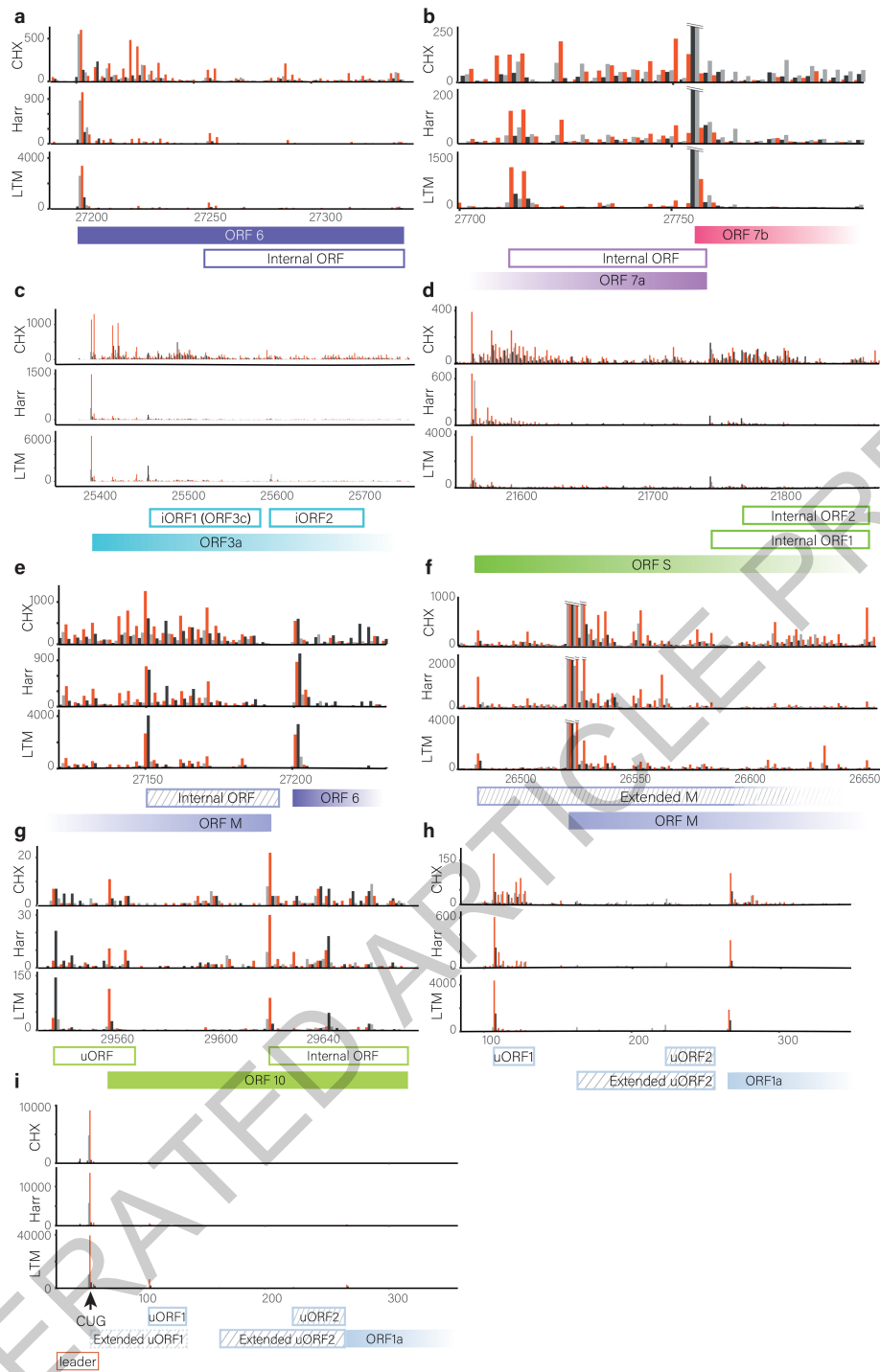


Fig. 3 | Ribosome densities reveal novel viral coding regions. **(A–I)** Ribosome density profiles of CHX, Harr and LTM samples at 5 hpi. Densities are shown with different colours indicating the frame relative to the main ORF (red, 0; black, +1; grey, +2). Filled and open rectangles indicate the canonical and novel ORFs, respectively. ORFs starting in a near cognate codon are labelled with stripes. **(A)** In-frame internal ORF within ORF6, **(B)** and within ORF7a. **(C)**

Out-of-frame internal initiations within ORF-3a, **(D)** within ORF-S, **(E)** and within ORF-M. **(F)** An extended version of ORF-M. **(G)** uORF that overlap ORF10 initiation and in-frame internal initiation generating truncated ORF10. **(H)** Two uORFs embedded in ORF1a 5'UTR. **(I)** Non canonical CUG initiation upstream of the TRS-leader. Reads that were cut to fit the scale are indicated with horizontal lines.

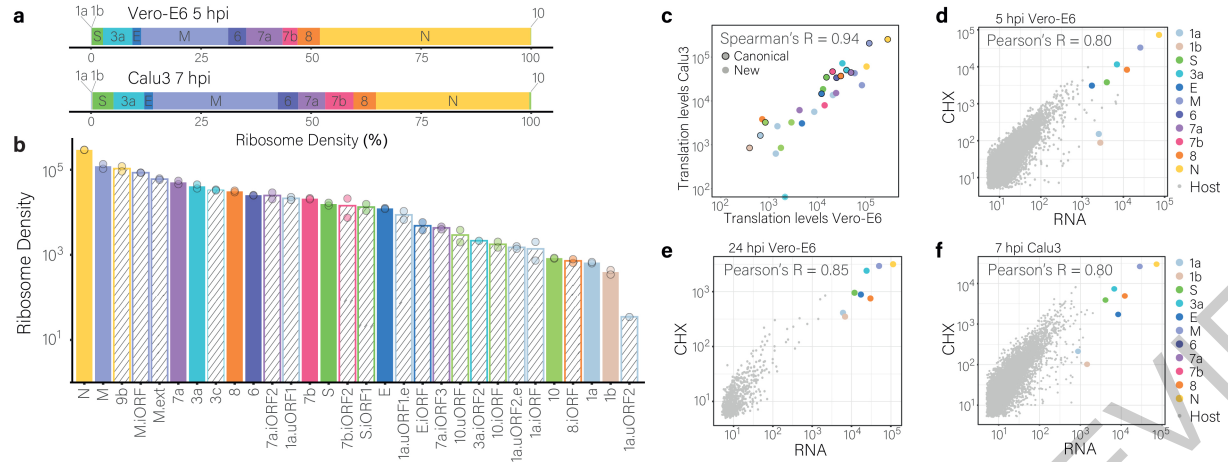


Fig. 4 | Translation of host and viral genes. **(A)** Translation levels of canonical viral ORFs for Vero at 5hpi and Calu3 at 7hpi. ORFs are ordered based on their genomic location. **(B)** Viral ORFs translation levels as calculated from ribosome densities for Vero Shpi. Solid fill represents canonical ORFs, and striped fill represents novel ORFs. **(C)** Scatter plot of viral ORF expression in Vero at 5hpi

and Calu3 at 7hpi. Points representing canonical ORFs are outlined in black. **(D-F)** Relative transcript abundance versus ribosome densities for each host and viral ORF at 5hpi **(D)** and 24hpi **(E)** in Vero and at 7hpi in Calu3 **(F)**. Transcript abundance was estimated by counting the reads that span the corresponding junction and footprint densities were calculated from the CHX sample.

Article

Methods

Cells and viruses

Vero C1008 (Vero E6) (ATCC CRL-1586) were cultured in T-75 flasks with DMEM supplemented with 10% fetal bovine serum (FBS), MEM non-essential amino acids, 2mM L-Glutamine, 100Units/ml Penicillin, 0.1mg/ml streptomycin, 12.5Units/ml Nystatin (Biological Industries, Israel). Calu3 cells (ATCC HTB-55) were cultured in 10cm plates with DMEM supplemented with 10% fetal bovine serum (FBS), MEM non-essential amino acids, 2mM L-Glutamine, 100Units/ml Penicillin, 1% non-essential amino acid and 1% Na-pyruvate. Caco-2 (ATCC HTB-37) were cultured in 10cm plates with DMEM supplemented with 20% fetal bovine serum (FBS), 1% GlutaMAX, 100Units/ml Penicillin, 0.1mg/ml streptomycin, and 1% Na-pyruvate. A549 cells (ATCC CCL-185) were cultured in 10cm plates with DMEM supplemented with 10% fetal bovine serum (FBS), 100Units/ml Penicillin, 0.1mg/ml streptomycin and 2mM L-Glutamine. Monolayers were washed once with DMEM (for VeroE6) or RPMI (for Calu3, A549 and Caco-2) without FBS and infected with SARS-CoV-2 virus, at a multiplicity of infection (MOI) of 0.2, For Calu3 infection 20 ug per ml TPCK trypsin (Thermo scientific) were added unless otherwise stated. After 1hr infection cells were cultured in their respective medium supplemented with 2% fetal bovine serum, and MEM non-essential amino acids, L glutamine and penicillin-streptomycin-Nystatin at 37 °C, 5% CO₂. SARS-CoV-2 (GISAID Acc. No. EPI_ISL_406862), was kindly provided by Bundeswehr Institute of Microbiology, Munich, Germany. It was propagated (4 passages) and tittered on Vero E6 cells and then sequenced (details below) before it was used. SARS-CoV-2 BavPat1/2020 Ref-SKU: 026V-03883 was kindly provided by Prof. C. Drosten, Charité – Universitätsmedizin Berlin, Germany. It was propagated (5 passages), tittered on Vero E6 and then sequenced before it has been used in experiments. Infected cells were harvested at the indicated times as described below. Handling and working with SARS-CoV-2 virus was conducted in a BSL3 facility in accordance with the biosafety guidelines of the Israel Institute for Biological Research. The Institutional Biosafety Committee of Weizmann Institute approved the protocol used in these studies.

Preparation of ribosome profiling and RNA sequencing samples

For RNA-seq, cells were washed with PBS and then harvested with Tri-Reagent (Sigma-Aldrich), total RNA was extracted, and poly-A selection was performed using Dynabeads mRNA DIRECT Purification Kit (Invitrogen) mRNA sample was subjected to DNaseI treatment and 3' dephosphorylation using FastAP Thermosensitive Alkaline Phosphatase (Thermo Scientific) and T4 PNK (NEB) followed by 3' adaptor ligation using T4 ligase (NEB). The ligated products used for reverse transcription with SSIII (Invitrogen) for first strand cDNA synthesis. The cDNA products were 3' ligated with a second adaptor using T4 ligase and amplified for 8 cycles in a PCR for final library products of 200-300bp. For Ribo-seq libraries, cells were treated with either 50µM lactimidomycin (LTM) for 30 min or 2µg/mL Harringtonine (Harr) for 5 min, for translation initiation libraries (LTM and Harr libraries correspondingly), or left untreated for the translation elongation libraries (cycloheximide [CHX] library). All three samples were subsequently treated with 100µg/mL CHX for 1 min. Cells were then placed on ice, washed twice with PBS containing 100µg/mL CHX, scraped from the T-75 flasks (Vero cells) or 10cm plates (Calu3 cells), pelleted and lysed with lysis buffer (1% triton in 20mM Tris 7.5, 150mM NaCl, 5mM MgCl₂, 1mM dithiothreitol supplemented with 10 U/ml Turbo DNase and 100µg/ml cycloheximide). After lysis samples stood on ice for 2h and subsequent Ribo-seq library generation was performed as previously described⁴. Briefly, cell lysate was treated with RNaseI for 45 min at room temperature followed by SUPERse-In quenching. Sample was loaded on sucrose solution (34% sucrose, 20mM Tris 7.5, 150mM NaCl, 5mM MgCl₂, 1mM dithiothreitol and 100µg/ml cycloheximide) and spun for 1h at 100K RPM using TLA-110 rotor (Beckman) at 4c. Pellet was harvested

using TRI reagent and the RNA was collected using chloroform phase separation. For size selection, 15µg of total RNA was loaded into 15% TBE-UREA gel for 65 min, and 28-34 footprints were excised using 28 and 34 flanking RNA oligos, followed by RNA extraction and ribo-seq protocol⁴

Virus genomic sequencing

RNA from viruses (culture supernatant after removal of cell debris) was extracted using viral RNA kit (Qiagen). The SMARTer Pico RNA V2 Kit (Clontech) was used for library preparation. Genome sequencing was conducted on the Illumina MiSeq platform, in a single read mode 60bp for BetaCoV/Germany/BavPat1/2020 EPI_ISL_406862 and in a paired-end mode 150bp x2 for BavPat1/2020 Ref-SKU: 026V-03883 producing 2,239,263 and 4,332,551 reads correspondingly. Reads were aligned to the viral genome using STAR 2.5.3a aligner. Even coverage along the genome was assessed and the relative abundance junctions (that may reflect genomic deletion) were calculated. For EPI_ISL_406862 passage 4 (that was used for Vero cells infection) the junctions that were found in more than 1% of genomes are listed in Supplementary Table 2. For BavPat1/2020 Ref-SKU: 026V-03883 passage 5 (that was used to for Calu3 infection) no junctions in abundance of more than 1% of the genomes were detected. All genomic sequencing data was deposited.

Sequence alignment, metagene analysis

Sequencing reads were aligned as previously described²⁸. Briefly, linker (CTGTAGGCACCATCAAT) and poly-A sequences were removed and the remaining reads from were aligned to the Chlorocebus sabaeus genome (ENSEMBL release 99) and to the SARS-CoV-2 genomes [Genbank NC_045512.2 with 3 changes to match the used strain (BetaCoV/Germany/BavPat1/2020 EPI_ISL_406862), 241:C→T, 3037:C→T, 23403:A→G]. (infection of Vero cells) or to the Hg19 and NC_045512.2 with the same sequence changes (infection of Calu3). Alignment was performed using Bowtie v1.1.2²⁹ with maximum two mismatches per read. Reads that were not aligned to the genome were aligned to the transcriptome of Chlorocebus sabaeus (ENSEMBL) and to SARS-CoV-2 junctions that were recently annotated¹². The aligned position on the genome was determined as the 5' position of RNA-seq reads, and for Ribo-seq reads the p-site of the ribosome was calculated according to reads length using the off-set from the 5' end of the reads that was calculated from canonical cellular ORFs. The offsets used are +12 for reads that were 28-29 bp and +13 for reads that were 30-33 bp. Reads that were in different length were discarded. In all figures presenting ribosome densities data all footprint lengths (28-33bp) are presented.

Novel junctions were mapped using STAR 2.5.3a aligner³⁰, with running flags as suggested at Kim et al., to overcome filtering of non-canonical junctions. Reads aligned to multiple locations were discarded. Junctions with 5' break sites mapped to genomic location 55-85 were assigned as leader-dependent junctions. Matching of leader junctions to ORFs, and categorization of junctions as canonical or non-canonical, was adapted from Kim et al.¹² Supplementary Table 3, or was assigned manually for strong novel junctions that appear only in our data.

For the metagene analysis only genes with more than 50 reads were used. For each gene normalization was done to its maximum signal and each position was normalized to the number of genes contributing to the position. In the virus 24hr samples, normalization for each gene was done to its maximum signal within the presented region.

Quantification of gene expression

The deconvolution of RNA expression was done by subtracting the RPKM of an ORF from the RPKM of the ORF located just upstream of it in the genome. The junction counts were based on STAR alignment number of uniquely mapped reads crossing the junction. For comparing transcript and footprint expression level, RNA and footprint counts from bowtie alignments were normalized to units of RPKM in order

to normalize for gene length and for sequencing depth. Based on the correlation between the deconvoluted RPKM and junction abundance of the subgenomic RNAs, the genomic RNA abundance was estimated and was used to estimate ORF1a and ORF1b RNA levels compared to footprint levels.

The estimation of the viral footprint densities from the 24 hpi samples was performed by calculating the ratio of the RPKM of ORF1a to the total number of leader canonical junctions at 5hpi. This ratio was used as a factor to calculate a proxy for the “true” viral footprint densities from the number of footprints that were mapped to leader canonical junctions at 24hpi.

To quantify the translation levels of novel viral ORFs at 5hpi and 7hpi, many of which are overlapping, three types of calculations were used based on ORF type. For ORFs that have a unique region, with no overlap to any other ORF, bowtie aligned read density was calculated in that region. For out-of-frame internal ORFs, the read density of the internal ORF region was calculated by estimating the expected 3-bp periodicity distribution of footprints based on non-overlapping translated regions in the main ORF. Using linear regression, we calculated the relative contribution of the frames of the main and of the internal ORF to the reads covering the region of the internal ORF. The relative contribution of the internal ORF was then multiplied by the read density in that region to obtain the estimated translation level of the internal out-of-frame ORF. For in-frame internal ORFs the read density of the main overlapping ORF is calculated from a non-overlapping region and then subtracted from the read density in the overlapping internal ORF region to get an estimate of translation levels of the internal ORF. In cases where the unique region used to calculate read density contained the start-codon of the ORF, the first 20% of the codons in the region were excluded from the calculation to avoid bias from initiation peaks, unless the region was very short and trimming it would harm the ability to estimate coverage (ORF 8 and extended ORF M). The exact regions that were used for calculation can be found in Supplementary Table 5. Finally, read density was normalized to the length of the region used for calculation and to the sum of length normalized reads in each sample to get TPM values. P-values for the relative contribution levels of out-of-frame ORFs were calculated from both replicates using a mixed-effects linear model using the 3-base periodicity distribution as the fixed effect and the replicates as random effect. In parallel, ORF-RATER was used to quantify the translation levels of the viral ORFs (using regression), giving largely similar values (Spearman’s $R=0.92$ and $R=0.87$ in VeroE6 and Calu3, respectively).

Prediction of translation initiation sites

Translation initiation sites were predicted using PRICE¹⁶ and ORF-RATER¹⁷. To estimate the codons generating the sequencing reads with maximum likelihood, PRICE requires a predefined set of annotated coding sequences from the same experiment. Thus, it does not perform well on reference sequences with a small number of annotated ORFs such as SARS-CoV-2. Since our experiment generated ribosome footprints from both SARS-CoV-2 and host mRNAs, which were exposed to the exact same conditions in the protocol, we used annotated CDSs from the host cells to evaluate the parameters of the experiment. For libraries of infected Vero cells sequencing reads were aligned using Bowtie to a fasta file containing chromosome 20 of *Chlorocebus sabaeus* (1240 annotated start codons, downloaded from ensembl: ftp://ftp.ensembl.org/pub/release99/fasta/chlorocebus_sabaeus/dna/) and the genomic sequence of SARS-CoV-2 (Refseq NC_045512.2). A gtf file with the annotations of *Chlorocebus sabaeus* and SARS-CoV-2 genomes was constructed and provided as the annotations file when running PRICE. For technical reasons, the annotation of the first coding sequence (CDS) of the two CDSs in the “ORF1ab” gene was deleted since having two CDSs encoded from a single gene was not permitted by PRICE. For libraries of infected Calu3 cells sequencing reads were mapped to a fasta file containing chromosome 1 of hg19 (2843 annotated start codons) and

the genomic sequence of SARS-CoV-2 (Refseq NC_045512.2). A gtf file with the annotations of hg19 and SARS-CoV-2 genomes was constructed and provided as the annotations file when running PRICE. For the data that was generated from infected Vero cells at 5hpi training and ORF prediction by PRICE were done once using the CHX data from both replicates, and again using all Ribo-seq libraries from both replicates, and the resulting predictions were combined. To test reproducibility, the same predictions were performed on each replicate separately. For the data that was generated from infected Calu3 cells at 7hpi training and ORF prediction by PRICE were done using all Ribo-seq libraries from both replicates. The predictions were further filtered to include only ORFs with at least 100 reads at the initiation site in the LTM samples of at least one replicate. ORFs were then defined by extending each initiating codon to the next in-frame stop codon.

ORF-RATER was used with the default values besides allowing all start codons with at most one mismatch to ATG. For each cell type, two runs of ORF-RATER were used. One in which ORF-RATER was trained on cellular annotations (chr 20 for the Vero cells, and chr 1 for the Calu cells) and SARS-CoV-2 canonical ORFs (similar to the procedure that was used for running PRICE). In the second run only SARS-CoV-2 canonical ORFs were used for training. In both cases ORF1b and ORF10 were omitted from the training set. BAM files from STAR alignment were used as input. The CHX data from both replicates was used in the first prune step to omit low coverage ORFs. The calculations of the P-site offsets, and the regression were performed for each Ribo-Seq library separately. The final score was calculated based on all three types of libraries. Score of 0.5 was used as cut-off for the final predictions these were further manually curated. Additional ORFs that were not recognized by the trained models (likely due to differences in the features of viral genome compared to cellular genomes) but presented reproducible translation profile in the two cell lines were added manually to the final ORF list (Supplementary Table 4). ORFs were manually identified as such if they had reproducible initiation peaks in the CHX libraries that were enhanced in the LTM and Harr libraries, and exhibited increased CHX signal in the correct reading-frame along the coding region.

Mapping reads to CUG initiation upstream the TRS-leader

Reads from ribosome profiling libraries were aligned using bowtie to a single reference that contained the transcripts and the genome allowing no mismatches or gaps. Reads with p-site mapped to position 59 of the viral genome were collected and divided to four groups according to the nucleotide in position +17 of the read (position 76 of the genome). The first group contains reads that are short (28 nucleotides) and do not have any nucleotide at position +17. The other three groups, referred to as T, A and G, correspond to combinations of genomic and subgenomic RNAs based on their sequence, as shown in Supplementary Fig. 14. Group T is attributed to the genome or to ORF E and ORF M subgenomic RNAs, group A to the subgenomic RNAs of ORF S, ORF7a, ORF8 and ORF N, and group G to the sub-genomic RNA of ORF 6. Reads mapped uniquely to the subgenomic RNA of ORF3a were excluded from calculation, and the number of reads in each group was summed. Group T, containing genomic reads, was further divided based on the nucleotide at position +18, where reads with A at that position can originate from the subgenomic RNA of ORF M and reads with T at that position can originate from the genome or from the subgenomic RNA of ORF E. Final division of the genomic group was done based on position +19 where T corresponds to genomic reads and A corresponds to ORF E subgenomic reads. RNA values as calculated from junction densities (described above) were summed for the subgenomic and genomic RNAs in each group. The analysis was performed for each ribosome profiling library separately.

Mining of proteomics data and transmembrane predictions

Data downloaded from Bojkova et al.⁸ was searched using Byonic search engine using 10ppm tolerance for MS1 and 20ppm tolerance

Article

for MS2, against the concatenated database containing our 26 novel ORFs as well as the human proteome DB (SwissProt Nov2019), and the SARS-CoV-2 proteome. Modifications allowed were fixed carbamidomethylation on C, fixed TMT6 on K and peptide N terminus, variable K8 and R10 SILAC labelling, variable M oxidation and Variable NQ deamidation. Data downloaded from Davidson et al.⁹ was searched using Byonic search engine using 10ppm tolerance for MS1 and 0.6Da tolerance for MS2, against the concatenated database containing our 26 novel ORFs as well as the human proteome DB (SwissProt Nov2019), and the SARS-CoV-2 proteome. Modifications allowed were fixed carbamidomethylation on C, variable N-terminal protein acetylation, M oxidation and NQ deamidation. Transmembrane and signal peptide predictions were performed using Phobius³¹.

Immunofluorescence

Cells were plated on ibidi slides, fixed in 3% paraformaldehyde for 20 min, permeabilized with 0.5% Triton X-100 in PBS for 2 min, and then blocked with 2% FBS in PBS for 30 min. Immunostaining was performed with rabbit anti-SARS-CoV-2 serum³² at a 1:200 dilution. Cells were washed and labelled with anti-rabbit FITC antibody and with DAPI (4 = ,6-diamidino-2-phenylindole) at a 1:200 dilution. Imaging was performed on a Zeiss AxioObserver Z1 wide-field microscope using a X40 objective and Axiocam 506 mono camera.

Reporting summary

Further information on research design is available in the Nature Research Reporting Summary linked to this paper.

Data availability

All next-generation sequencing data files were deposited in Gene Expression Omnibus under accession number GSE149973. All the RNA-seq and ribosome profiling data generated in this study can be accessed through a UCSC browser session: <http://genome.ucsc.edu/s/>

aharonn/CoV2%2DTranslation. The proteomics data analysed in this study are available in PRIDE repository with the identifiers PXD017710⁸ and PDX018241⁹.

28. Tirosch, O. et al. The Transcription and Translation Landscapes during Human Cytomegalovirus Infection Reveal Novel Host-Pathogen Interactions. *PLoS Pathog.* **11**, e1005288 (2015).
29. Langmead, B., Trapnell, C., Pop, M. & Salzberg, S. L. Ultrafast and memory-efficient alignment of short DNA sequences to the human genome. *Genome Biol.* **10**, R25 (2009).
30. Dobin, A. et al. STAR: ultrafast universal RNA-seq aligner. *Bioinformatics* **29**, 15–21 (2013).
31. Käll, L., Krogh, A. & Sonnhammer, E. L. L. A combined transmembrane topology and signal peptide prediction method. *J. Mol. Biol.* **338**, 1027–1036 (2004).
32. Yahalom-Ronen, Y. et al. A single dose of recombinant VSV-ΔG-spike vaccine provides protection against SARS-CoV-2 challenge. *bioRxiv* 2020.06.18.160655 (2020). <https://doi.org/10.1101/2020.06.18.160655>.

Acknowledgements We thank Stern-Ginossar lab members, Igor Ulitsky and Schraga Schwartz for providing valuable feedback, to Eran Zehavi, Miri Shnayder, Igor Ulitsky and Noa Gil for technical assistance. We thank Emanuel Wyler for the Calu3 cells. We thank Inbar Cohen-Gihon for sharing sequencing and bioinformatics data. This study was supported by the Ben B. and Joyce E. Eisenberg Foundation. Work in the Stern-Ginossar lab is supported by ERC-CoG-2019- 864012 and by the ISF grant no. 1526/18. S.W.G. is the recipient of the HSPF fellowship, EMBO non-stipendiary Long-Term Fellowship, the Gruss-Lipper Postdoctoral Fellowship, the Zuckerman STEM Leadership Program and the Rothschild Postdoctoral Fellowship. N.S.-G is an incumbent of the Skirball Career Development Chair in New Scientists and is a member of EMBO Young Investigator Program. The authors declare no competing interests.

Author contributions Y.F., O.M., N.P and N.S.-G. conceptualization. O.M. experiments, Y.F., A.N. and S.W.G. data analysis. YY-R., H.T., H.A., S.M., S.W., I.C-G, D.S, O.I, A. B-D, T.I. and N.P. work with SARS-CoV-2. D.M mined published proteomic data, Y.F., O.M., A.N., M.S. and N.S.-G. interpreted data. M.S. and N.S.-G. wrote the manuscript with contribution from all other authors.

Competing interests The authors declare no competing interests.

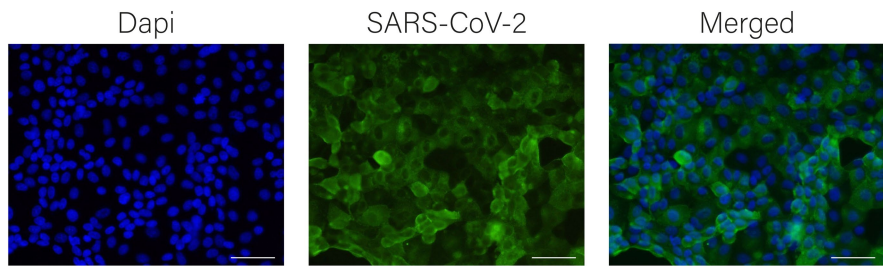
Additional information

Supplementary information is available for this paper at <https://doi.org/10.1038/s41586-020-2739-1>.

Correspondence and requests for materials should be addressed to N.S.-G.

Peer review information *Nature* thanks Volker Thiel, Petra Van Damme and the other, anonymous, reviewer(s) for their contribution to the peer review of this work. Peer reviewer reports are available.

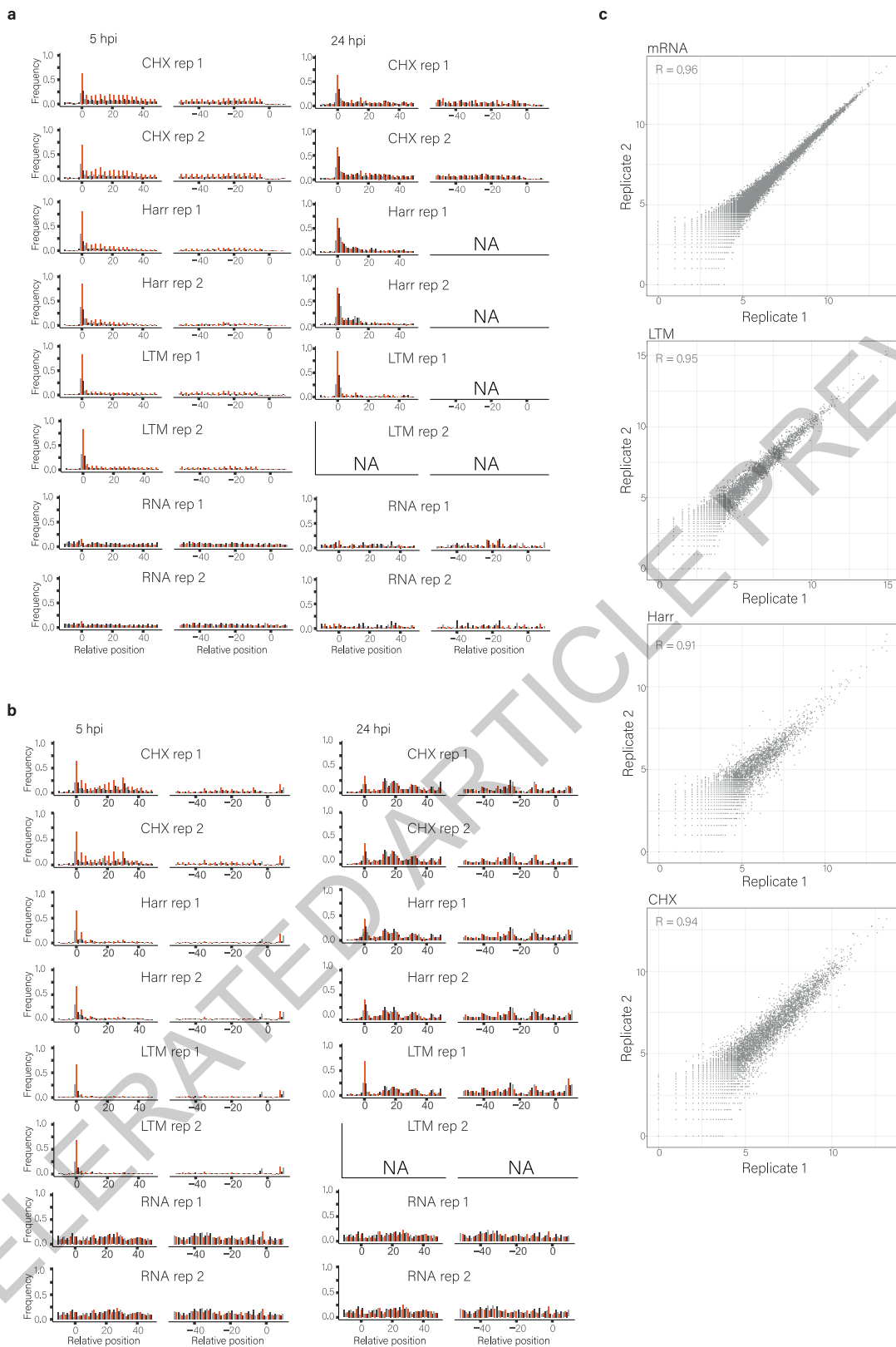
Reprints and permissions information is available at <http://www.nature.com/reprints>.



Extended Data Fig. 1 | 24 h infection with SARS-CoV-2 of Vero E6 cells. Vero E6 cells were infected with SARS-CoV-2 at an MOI = 0.2 and 24 hpi the cells were fixed and stained with antisera against SARS-CoV-2 (green) and Dapi (blue). The

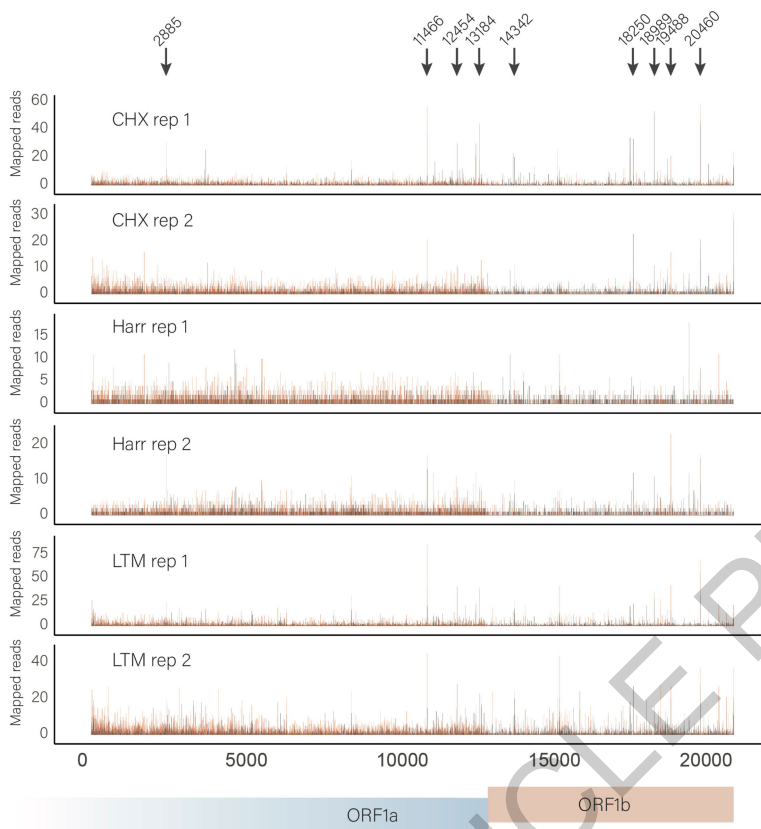
experiment was performed once and representative microscopy images are presented. Scale bars are 200 μ m.

ACCELERATED ARTICLE PREVIEW



Extended Data Fig. 2 | Footprint and RNA-seq profiles of cellular and viral genes from SARS-CoV-2 infected Vero E6 cells. (a and b) Metagene analysis of read densities at the 5' and the 3' regions of cellular (a) and viral (b) protein coding genes as measured by the different ribosome profiling approaches and RNA-seq at 5hpi and 24hpi, from two biological replicates. The X axis shows the nucleotide position relative to the start or the stop codons. The ribosome densities are shown with different colours indicating the three frames relative

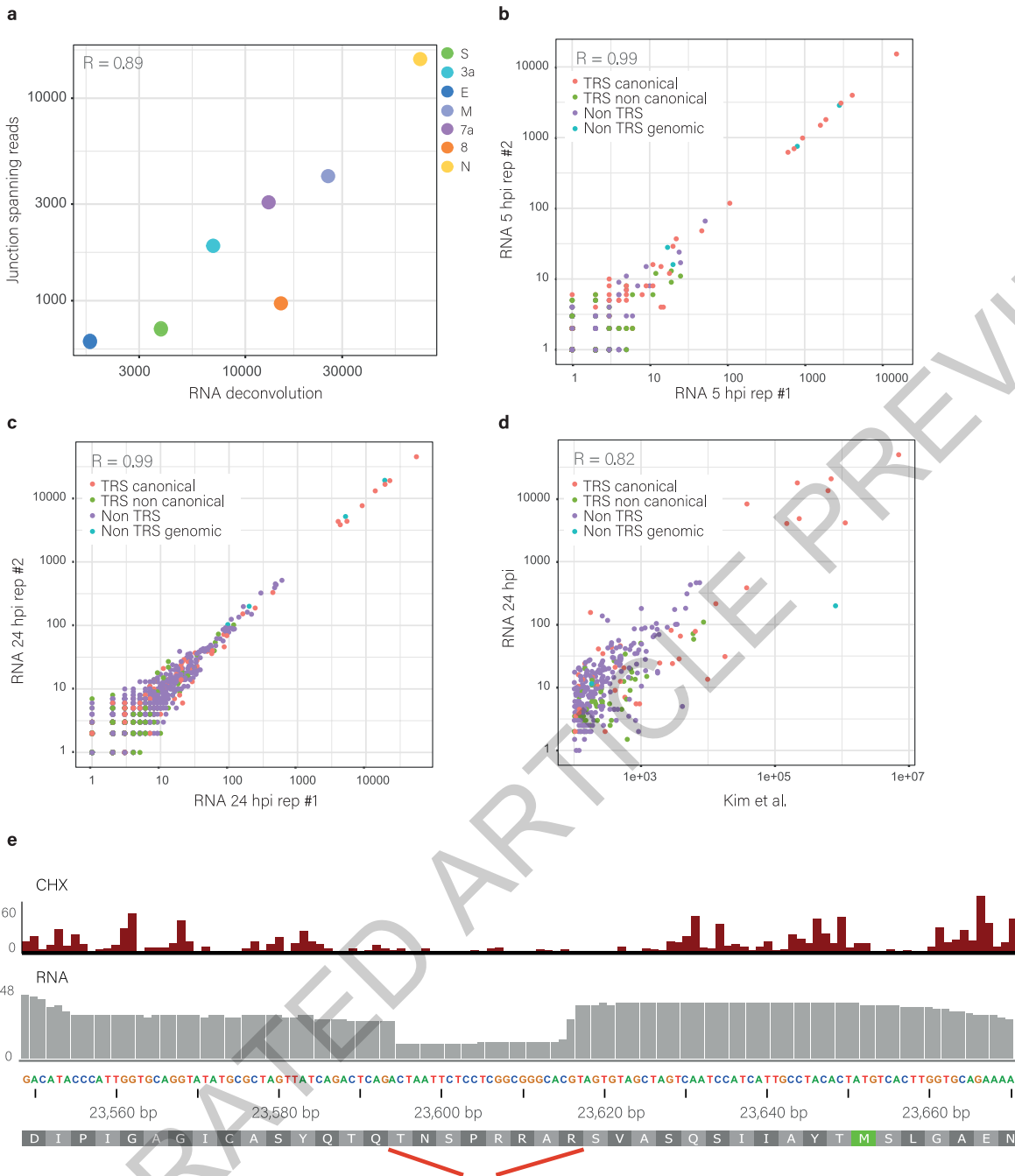
to the main ORF (red, frame 0; black, frame +1; grey, frame +2). NA reflect samples in which we did not obtain enough cellular genes that contain 50 reads at the 5' or 3' regions to generate metagene profile. (c) Scatter plots depicting the number of reads in every position along the SARS-CoV-2 genome in two independent biological replicates, demonstrating reproducibility between our replicates at single nucleotide resolution. Pearson's R of log transformed values is presented.



Extended Data Fig. 3 | Footprint profiles reveal potential ribosome pausing sites within ORF1a and ORF1b. Read densities are presented for ORF1a and ORF1b at 5 hpi from two biological replicates. The ribosome densities are

shown with different colours indicating the three frames relative to the translated frame of ORF1a (red, frame 0; black, frame +1; grey, frame +2). Black arrows mark potential ribosome pausing sites and their genomic positions.

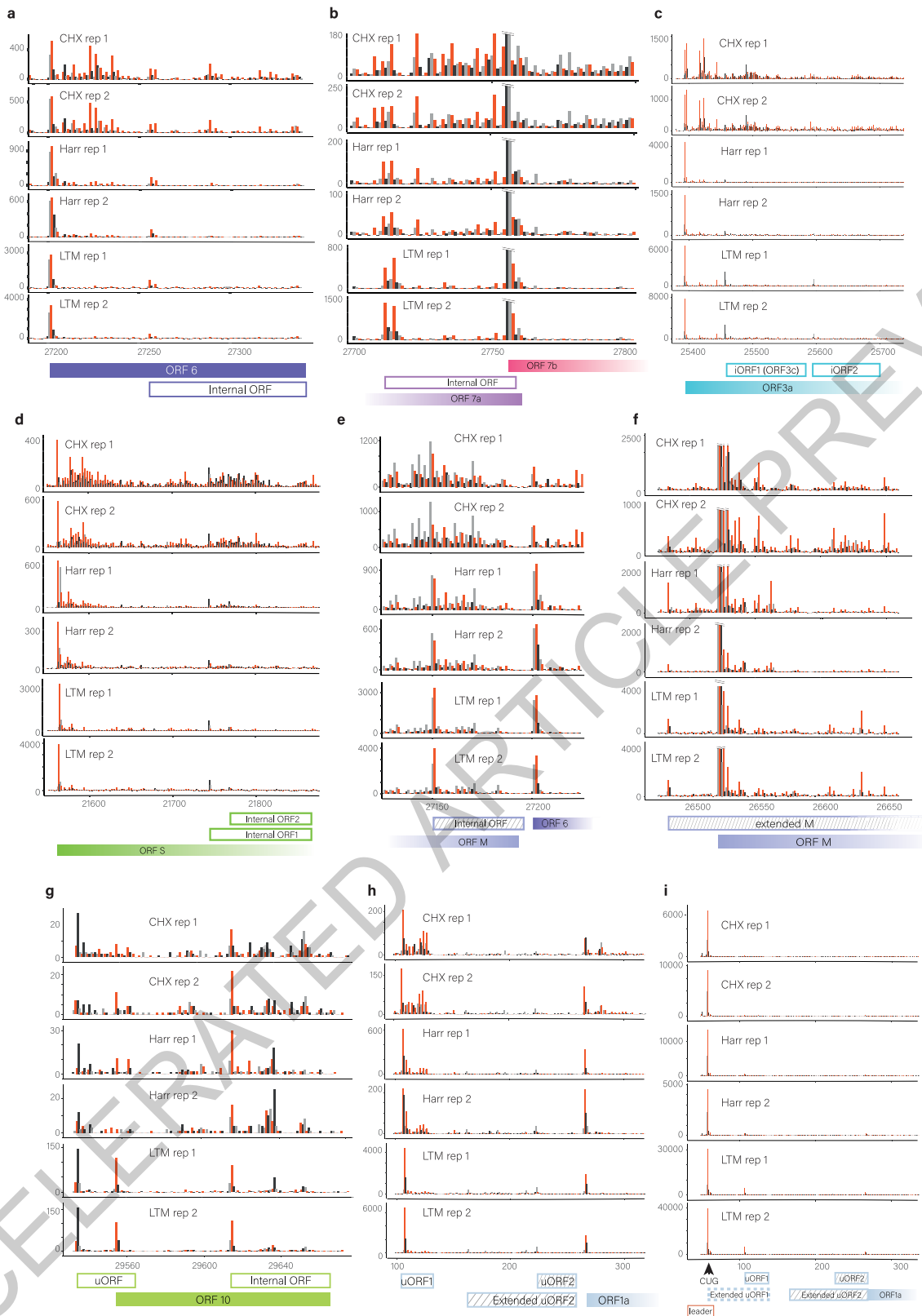
Article



Extended Data Fig. 4 | The abundance of subgenomic RNAs. (a)

Measurement of subgenomic RNA abundance using deconvolution of RNA densities versus using relative abundance of RNA reads spanning leader-body junctions, for seven canonical viral ORFs. ORF6, ORF7b and ORF10 obtained negative values in the RNA deconvolution, probably due to their short length and relative weaker expression. For ORF10 also no reads spanning leader-body junctions were detected. Spearman's R is presented. (b and c) Scatter plots presenting the abundance of junction-spanning RNA-seq reads from two biological replicates from (b) Shpi and (c) 24hpi. (d) Scatter plots presenting the average abundance of junction-spanning RNA-seq reads from 24hpi versus

data from Kim et al. Viral reads that span canonical leader dependent junctions are marked in red, non-canonical leader dependent junctions are marked in green, non-canonical leader independent junctions are marked in purple and non-canonical leader independent junctions originating from genomic deletions are marked in cyan. Pearson's R of log transformed values is presented. (e) Ribosome profiling (CHX) and RNA densities over the 7aa deletion in the S protein. Lower panels present the amino acid sequence in the region and the translation of the WT and of the 7aa deleted version of the S protein.

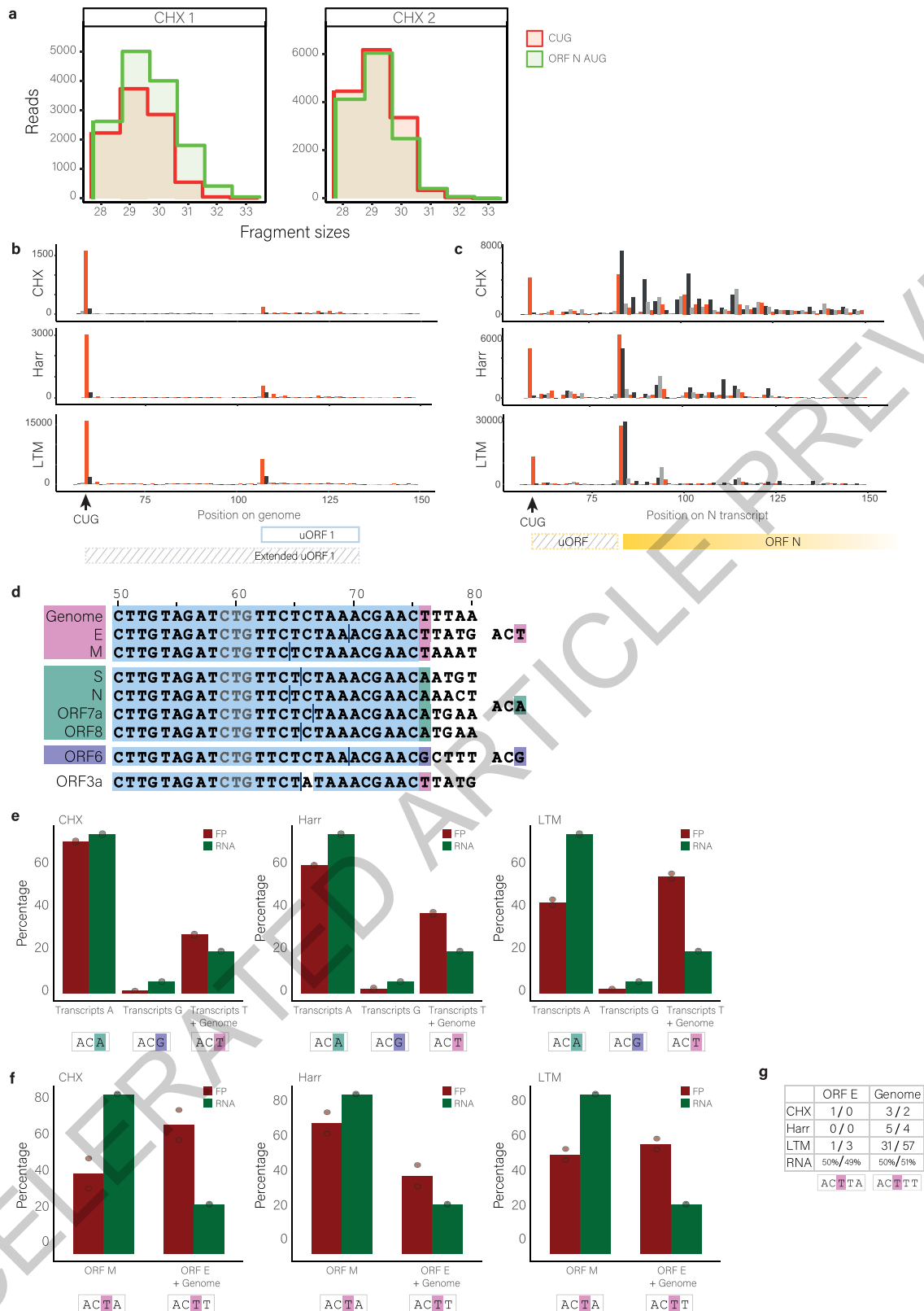


Extended Data Fig. 5 | Footprint profiles reveal novel viral coding regions.

(a-i) Read densities over SARS-CoV-2 unannotated translated ORFs as measured by the different ribosome profiling approaches from both replicates at Shpi. The ribosome densities are shown with different colours indicating the three frames relative to the main ORF in each figure (red, frame 0; black, frame +1; grey, frame +2). Filled and open rectangles indicate the canonical and novel ORFs, respectively. ORFs starting in near cognate start codon are labelled with

stripes. (a) In frame internal initiation within ORF6 generating truncated product. (b) In frame internal initiation within ORF7a. (c) Out of frame internal initiations within ORF3a. (d) Out of frame internal initiations within ORF-S. (e) Out of frame internal initiation within ORF-M. (f) an extended version of ORF-M. (g) uORF that overlaps ORF10 initiation and in frame internal initiation generating truncated ORF10 product. (h) two uORFs embedded in ORF1ab 5'UTR. (i) non-canonical CUG initiation upstream of the TRS leader.

Article



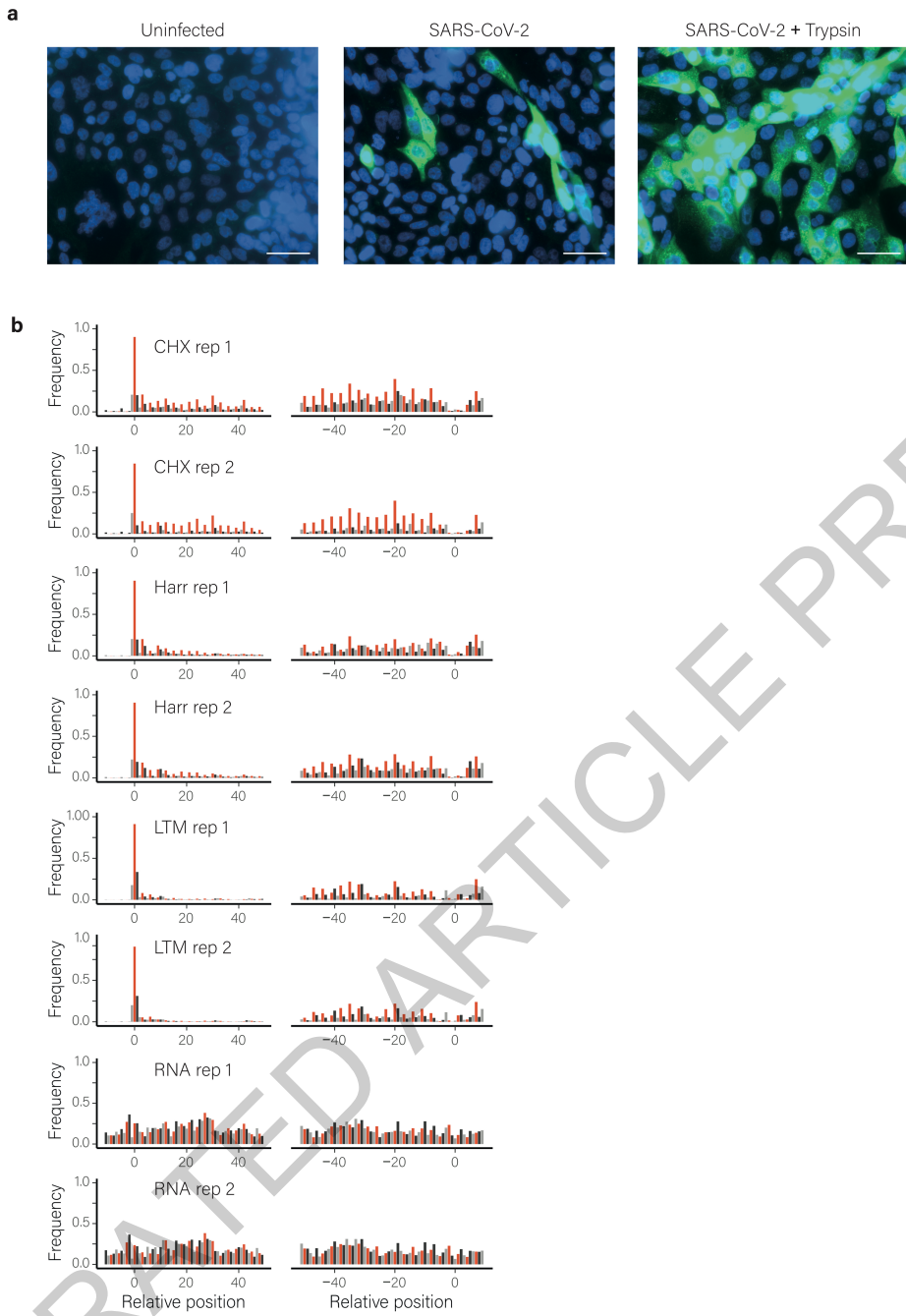
Extended Data Fig. 6 | See next page for caption.

Extended Data Fig. 6 | The CUG initiation is enriched on the genomic RNA.

(a) Comparison of the ribosome footprint read length distributions of reads that align to the CUG upstream of the TRS-L (red) and reads that align to ORF-N AUG (green). **(b and c)** Read densities over the TRS-L CUG on the genomic RNA (**b**) or ORF-N transcript (**c**) as measured by the different ribosome profiling approaches at Shpi. The ribosome densities are shown with different colours indicating the three frames relative to the CUG (red, frame 0; black, frame +1; grey, frame +2). Rectangles indicate adjacent ORFs and the striped rectangles indicate the ORFs initiating at the TRS-L CUG. **(d)** The sequences of the genome and the most abundant subgenomic transcripts divided to three groups based on the base in position 76. The CUG position is labelled in grey and the location of the junction is labelled by a vertical line. **(e)** The relative number of footprint reads that their P-site was mapped to the CUG (dark red) for each of the

transcript groups (as defined in C) and the relative RNA abundance of these transcript groups (green). Data are presented for CHX, Harr and LTM libraries.

(f) The relative number of footprint reads that their P-site was mapped to the CUG (dark red) in ORF-M transcript or in ORF-E and the Genome RNA and the relative RNA abundance (green). Only footprint sizes 31-33bp that allow unique alignment were used. Data are presented for CHX, Harr and LTM libraries. **(g)** The number of footprint reads that their P-site was mapped to the CUG in the genome or in ORF-E transcript out of all reads and the relative abundance of these RNAs. Only footprint sizes 32-33bp that allow unique alignment were used. Read numbers is presented for CHX, Harr and LTM libraries and the relative RNA abundance is presented as percentage of total RNA included in the comparison.



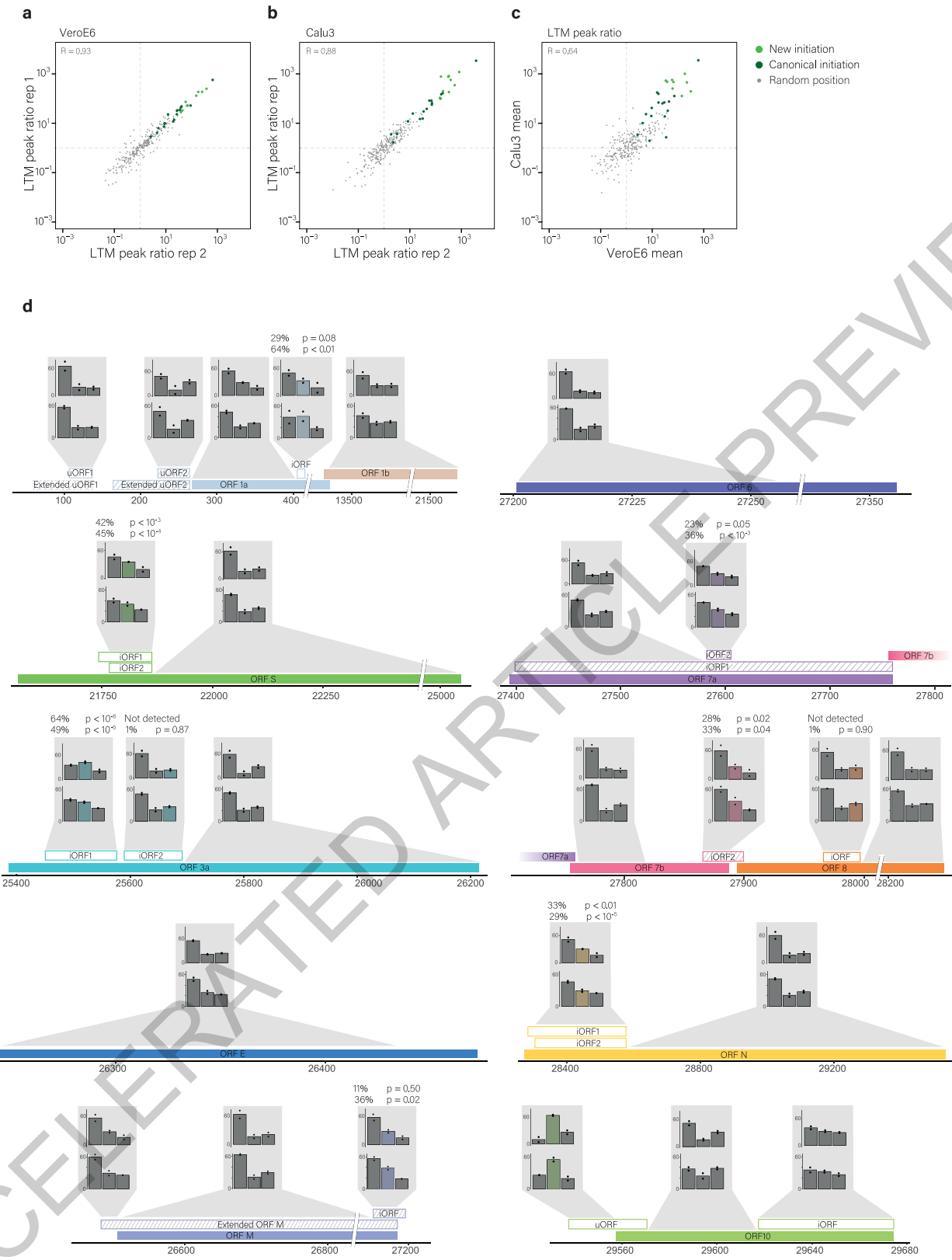
Extended Data Fig. 7 | SARS-CoV-2 infection of Calu3 cells. (a) Calu3 cells were either left uninfected, infected with SARS-CoV-2, or infected with SARS-CoV-2 in the presence of trypsin. 12hpi the cells were fixed and stained with antisera against SARS-CoV-2 (green) and Dapi (blue). The experiment was performed once and representative microscopy images are presented. Scale bars are 200 μ m. (b) Metagene analysis of read densities at the 5' and the 3'

regions of viral protein coding genes as measured by the different ribosome profiling approaches and RNA-seq at 7hpi from two biological replicates. The X axis shows the nucleotide position relative to the start or the stop codons. The ribosome densities are shown with different colours indicating the three frames relative to the main ORF (red, frame 0; black, frame +1; grey, frame +2).



Extended Data Fig. 8 | Footprint profiles reveal novel viral coding regions are also translated in infected Calu3 cells. (a-i) Read densities over SARS-CoV-2 unannotated translated ORFs as measured by the different ribosome profiling approaches from both replicates at 7hpi. The ribosome densities are shown with different colours indicating the three frames relative to the main ORF in each figure (red, frame 0; black, frame +1; grey, frame +2). Filled and open rectangles indicate the canonical and novel ORFs, respectively. ORFs starting in near cognate start codon are labelled with stripes. (a) In frame

internal initiation within ORF6 generating truncated product. (b) In frame internal initiation within ORF7a. (c) Out of frame internal initiation within ORF3a. (d) Out of frame internal initiation within ORF-S. (e) Out of frame internal initiation within ORF-M. (f) an extended version of ORF-M. (g) uORF that overlap ORF10 initiation and in frame internal initiation generating truncated ORF10 product. (h) Two uORFs embedded in ORF1ab 5'UTR. (i) non-canonical CUG initiation upstream of the TRS-leader.



Extended Data Fig. 9 | See next page for caption.

Extended Data Fig. 9 | Reproducibility of viral ORFs translation. Scatter plot presenting the correlation of footprint densities at each initiation site relative to a 8bp window 3 nucleotides downstream of the initiation site in LTM treated samples between two biological replicates of infected Vero E6, 5hpi (**a**), between two biological replicates of infected Calu3 cells, 7hpi (**b**) and between infected Vero E6 cells at 5hpi and Calu3 cells at 7hpi (**c**). Canonical ORFs are marked in dark green and newly identified ORFs are marked in light green. As a control, the relative occupancy of random positions was calculated in the same way (grey). Dashed lines mark the equal ratio of one. Spearman's R is presented. (**d**) The position of ribosome footprints relative to the reading frame in all canonical ORFs and novel ORFs excluding in-frame internal ORFs are presented for our measurements of infected Vero-E6 cells at 5hpi (lower panels) and infected Calu3 cells (upper panels). Filled and open rectangles indicate the canonical and novel ORFs, respectively. ORFs starting in near cognate start

codons are labelled with stripes. The frame of the footprints is summed on each of the indicated regions and is presented relative to the frame of the canonical ORF in each of these loci. In all non-overlapping regions, beside ORF10 in Vero-E6 cells, clear enrichment to the translated frame is observed indicating active translation. For out-of-frame overlapping ORFs the bar of its frame is labelled by colour and the percentage of the footprints that originate from the overlapping frame as was calculated from linear regression is presented together with the corresponding P-value for the contribution of the out-of-frame ORF to the frame distribution of the total reads in this region, using two degrees of freedom that reflect the two replicates. In two out-of-frame overlapping ORFs, ORF3.iORF2 and ORF8.iORF the expression relative to the main ORF was low and did not lead to a significant shift in the translation signal. In all other ORFs there is a significant signal in the alternative frame indicating active translation.



Extended Data Fig. 10 | See next page for caption.

Extended Data Fig. 10 | Characteristics of novel predicted ORFs. (a-b)

Scatter plots presenting the correlation between translation levels as estimated by our curated quantification and as calculated by ORF-RATER for Vero (a) and Calu3 cells (b). Points representing canonical ORFs are outlined in black. Spearman's R is presented. (c-d) Read densities over ORF-NAs measured by the different ribosome profiling approaches in two replicates in (c) Vero cells at 5hpi and (d) Calu3 cells at 7hpi. The ribosome densities are shown with different colours indicating the three frames relative to the main ORF in each figure (red, frame 0; black, frame +1; grey, frame +2). Filled and open rectangles indicate the canonical and novel ORFs, respectively. ORF14 location is marked

based on the homology to SARS-CoV. (e) Transmembrane region predicted in S.iORF1 using Phobius (f) Transmembrane region predicted in ORF3c (3a.iORF1) using Phobius (g) signal peptide prediction in 3a.iORF2 as predicted using Phobius. (h-i) Read densities over ORF3a as measured by the different ribosome profiling approaches in two replicates in (h) Vero cells at 5hpi and (i) Calu3 cells at 7hpi. The ribosome densities are shown with different colours indicating the three frames relative to the main ORF in each figure (red, frame 0; black, frame +1; grey, frame +2). Filled and open rectangles indicate the canonical and novel ORFs, respectively. ORF3b and extended iORF2 are marked based on the homology to SARS-CoV.

Reporting Summary

Nature Research wishes to improve the reproducibility of the work that we publish. This form provides structure for consistency and transparency in reporting. For further information on Nature Research policies, see our [Editorial Policies](#) and the [Editorial Policy Checklist](#).

Statistics

For all statistical analyses, confirm that the following items are present in the figure legend, table legend, main text, or Methods section.

n/a Confirmed

- The exact sample size (n) for each experimental group/condition, given as a discrete number and unit of measurement
- A statement on whether measurements were taken from distinct samples or whether the same sample was measured repeatedly
- The statistical test(s) used AND whether they are one- or two-sided
Only common tests should be described solely by name; describe more complex techniques in the Methods section.
- A description of all covariates tested
- A description of any assumptions or corrections, such as tests of normality and adjustment for multiple comparisons
- A full description of the statistical parameters including central tendency (e.g. means) or other basic estimates (e.g. regression coefficient) AND variation (e.g. standard deviation) or associated estimates of uncertainty (e.g. confidence intervals)
- For null hypothesis testing, the test statistic (e.g. F , t , r) with confidence intervals, effect sizes, degrees of freedom and P value noted
Give P values as exact values whenever suitable.
- For Bayesian analysis, information on the choice of priors and Markov chain Monte Carlo settings
- For hierarchical and complex designs, identification of the appropriate level for tests and full reporting of outcomes
- Estimates of effect sizes (e.g. Cohen's d , Pearson's r), indicating how they were calculated

Our web collection on [statistics for biologists](#) contains articles on many of the points above.

Software and code

Policy information about [availability of computer code](#)

Data collection no software was used for data collection

Data analysis For alignments we used Bowtie v1.1.2 and STAR 2.5.3a aligner. For ORF prediction we used PRICE 1.0.3 algorithm and ORF-RATER downloaded at April 2020 from <https://github.com/alexfIELDS/ORF-RATER>.
For signal peptide prediction and transmembrane domain prediction Phobius 1.01.

For manuscripts utilizing custom algorithms or software that are central to the research but not yet described in published literature, software must be made available to editors and reviewers. We strongly encourage code deposition in a community repository (e.g. GitHub). See the Nature Research [guidelines for submitting code & software](#) for further information.

Data

Policy information about [availability of data](#)

All manuscripts must include a [data availability statement](#). This statement should provide the following information, where applicable:

- Accession codes, unique identifiers, or web links for publicly available datasets
- A list of figures that have associated raw data
- A description of any restrictions on data availability

All next-generation sequencing data files were deposited in Gene Expression Omnibus under accession number GSE149973.

All the data generated in this study can be accessed through a UCSC browser session: <http://genome.ucsc.edu/s/aharonn/CoV2%2DTranslation>

The proteomics data analyzed in this study are available in PRIDE repository with the identifiers PXD017710 and PDX018241

Field-specific reporting

Please select the one below that is the best fit for your research. If you are not sure, read the appropriate sections before making your selection.

Life sciences

Behavioural & social sciences

Ecological, evolutionary & environmental sciences

For a reference copy of the document with all sections, see nature.com/documents/nr-reporting-summary-flat.pdf

Life sciences study design

All studies must disclose on these points even when the disclosure is negative.

Sample size	No calculation were performed for sample size selection. We prepared libraries for biological duplicates, as is customary in the field, and found excellent correlation between duplicated, as shown in figures S2, S4 and S9 in direct comparison, as well as in figures S5 and S8.
Data exclusions	We did not exclude data, other than a few point cases that are specified in the text. Data was only excluded when no signal was detected, and then it is indicated as NA or a missing point and described in the legend.
Replication	We confirmed there is strong correlation between duplicates, and between results from a different cell type, viral isolate and time point
Randomization	Tissue culture grown cells were randomly assigned treatments
Blinding	Blinding was not relevant to the study since we did not compare between groups

Reporting for specific materials, systems and methods

We require information from authors about some types of materials, experimental systems and methods used in many studies. Here, indicate whether each material, system or method listed is relevant to your study. If you are not sure if a list item applies to your research, read the appropriate section before selecting a response.

Materials & experimental systems		Methods	
n/a	Involved in the study	n/a	Involved in the study
<input type="checkbox"/>	<input checked="" type="checkbox"/> Antibodies	<input checked="" type="checkbox"/>	<input type="checkbox"/> ChIP-seq
<input type="checkbox"/>	<input checked="" type="checkbox"/> Eukaryotic cell lines	<input checked="" type="checkbox"/>	<input type="checkbox"/> Flow cytometry
<input checked="" type="checkbox"/>	<input type="checkbox"/> Palaeontology and archaeology	<input checked="" type="checkbox"/>	<input type="checkbox"/> MRI-based neuroimaging
<input checked="" type="checkbox"/>	<input type="checkbox"/> Animals and other organisms		
<input checked="" type="checkbox"/>	<input type="checkbox"/> Human research participants		
<input checked="" type="checkbox"/>	<input type="checkbox"/> Clinical data		
<input checked="" type="checkbox"/>	<input type="checkbox"/> Dual use research of concern		

Antibodies

Antibodies used	Hyperimmune rabbit serum from intravenous (i.v.) SARS-CoV-2 infected rabbits was used at a 1:200 dilution. Goat anti-rabbit FITC (Sigma #F6005, lot#107K6086) was used at a 1:200 dilution
Validation	Specificity was validated by staining SARS-CoV-2 infected cells in parallel to mock infected cells. Staining was specific to infected cells, no staining was observed in mock infected cells. The specificity of the secondary antibody was validated without primary antibody which showed no signal.

Eukaryotic cell lines

Policy information about [cell lines](#)

Cell line source(s)	VERO-E6 (ATCC CRL-1586), Calu-3 (ATCC HTB-55), A549 (ATCC CCL-185) and Caco-2 (ATCC HTB-37) cells were purchased from ATCC
Authentication	All cell lines were purchased and authenticated from ATCC
Mycoplasma contamination	All cell lines were tested negative for Mycoplasma
Commonly misidentified lines (See ICLAC register)	None